Journal of Nuclear Medicine, published on July 15, 2011 as doi:10.2967/jnumed.111.089953

# Imaging of the Striatal and Extrastriatal Dopamine Transporter with $^{18}$F-LBT-999: Quantification, Biodistribution, and Radiation Dosimetry in Nonhuman Primates

Andrea Varrone[1], Vladimir Stepanov[1], Ryuji Nakao[1], Miklós Tóth[1], Balázs Gulyás[1], Patrik Emond[2], Jean Bernard Deloye[3], Johnny Vercouillie[2], Michael G. Stabin[4], Cathrine Jonsson[5], Denis Guilloteau[*2], and Christer Halldin[*1]

[1]*Karolinska Institutet, Department of Clinical Neuroscience, Centre for Psychiatry Research, Stockholm, Sweden;* [2]*INSERM U930, CHRU Tours, Tours, France;* [3]*Laboratoires Cyclopharma, Saint Beauzire, France;* [4]*Department of Radiology and Radiological Sciences, Vanderbilt University, Nashville, Tennessee; and* [5]*Department of Nuclear Medicine, Karolinska Hospital, Stockholm, Sweden*

The aim of this study was to evaluate the quantification, biodistribution, and radiation dosimetry of the novel dopamine transporter (DAT) radioligand $^{18}$F-(2*S*,3*S*)-methyl 8-((*E*)-4-fluoro-but-2-en-1-yl)-3-(*p*-tolyl)-8-azabicyclo[3.2.1]octane-2-carboxylate ($^{18}$F-LBT-999) in nonhuman primates. **Methods:** The brain study was conducted in 4 female rhesus monkeys. PET measurements were conducted for 243 min using the high-resolution research tomograph (HRRT) with the measurement of the metabolite-corrected arterial input function and protein binding. Quantification was performed with kinetic analysis using 2-tissue- and 1-tissue-compartment models, with Logan graphical analysis and with different reference tissue models. The outcome measures were total distribution volume ($V_T$), nondisplaceable distribution volume ($V_{ND}$), binding potential relative to the free concentration of radioligand in plasma ($BP_F$), and binding potential relative to the concentration of nondisplaceable radioligand in tissue ($BP_{ND}$) = $V_T - V_{ND}/V_{ND}$ using the cerebellum as a reference region. For the biodistribution and radiation dosimetry, 2 female cynomolgus monkeys were studied. Whole-body PET scans were obtained using a PET/CT system for approximately 250 min. Estimates of the absorbed radiation dose in humans were calculated using OLINDA/EXM software. **Results:** $^{18}$F-LBT-999 showed good brain uptake (300% standardized uptake value) and regional distribution according to known DAT density. The 2-tissue-compartment model was the preferred model for the quantification. Late peak equilibrium (120–140 min) and slow washout were observed in the striatum, with high variability of $V_T$, $BP_F$, and $BP_{ND}$. When the different models were compared with the 2-tissue-compartment model, the underestimation of $V_T$ or $BP_{ND}$ was larger in the caudate and putamen than in the midbrain and thalamus. The reference tissue models were suitable for the quantification. The whole-body distribution study showed that the main routes of excretion of $^{18}$F-LBT-999 were the urinary and gastrointestinal systems, with the bladder being the critical organ. Accumulation of $^{18}$F-LBT-999 was found in the bone and skull, with a relatively high dose estimated for the osteogenic cells. The range of calculated effective dose was 0.021–0.022 mSv/MBq. **Conclusion:** $^{18}$F-LBT-999 seemed to be a suitable PET radioligand for the DAT quantification, particularly for extrastriatal regions. The skull uptake did not seem to be a limitation for brain imaging. The calculated dosimetry estimates based on data in nonhuman primates seemed comparable with those of other clinically used $^{18}$F-labeled radioligands, for example, $^{18}$F-FDG (0.024–0.027 mSv/MBq).

**Key Words:** PET; radiobiology/dosimetry; radiotracer tissue kinetics; dopamine transporter; reference tissue method

**J Nucl Med 2011; 52:1313–1321**
DOI: 10.2967/jnumed.111.089953

Dopamine is one of the main monoamine neurotransmitters involved in the regulation of important brain functions, such as locomotor activity, reward, and cognition (*1*). The dopamine transporter (DAT) is the plasma membrane protein that acts by clearing dopamine released into the extracellular space. The highest density of the DAT protein is in the striatum and nucleus accumbens, followed by the mesencephalic dopamine neurones of substantia nigra and ventral tegmental area (*2*). DAT imaging has been used for several studies in neurodegenerative and psychiatric disorders characterized by the involvement of the dopamine system (*3*). In Parkinson disease (PD), imaging of the DAT in the striatum might serve as a diagnostic marker of dopamine deficit. In PD, the substantia nigra is the region in which the primary pathology of the disorder occurs, and abnormalities in the DAT availability in the midbrain and the thalamus have been shown in attention-deficit hyperactivity disorders and schizophrenia (*4,5*). Therefore, the development of radioligands able to quantify the DAT availability in brain regions with higher and lower DAT density has a potential for application in neurodegenerative and psychiatric disorders. In addition, the development of

Received Mar. 3, 2011; revision accepted Apr. 20, 2011.
For correspondence or reprints contact: Andrea Varrone, Karolinska Institutet, Department of Clinical Neuroscience, Centre for Psychiatry Research, R5:02, Karolinska Hospital, SE-17176, Stockholm, Sweden.
E-mail: andrea.varrone@ki.se
*Contributed equally to this work.

an $^{18}$F-labeled radioligand would be an advantage for routine application and large clinical studies.

((2*S*,3*S*)-methyl 8-((*E*)-4-fluorobut-2-en-1-yl)-3-(*p*-tolyl)-8-azabicyclo[3.2.1]octane-2-carboxylate (LBT-999) is a tropane derivative with high affinity for the DAT (radioligand equilibrium dissociation constant [$K_D$], 9.15 nM) (*6*), and similarly to PE2I, LBT-999 is of potential interest for imaging the DAT in the striatum and extrastriatal regions (*7*). LBT-999 has been labeled with both $^{11}$C and $^{18}$F (*8–10*). $^{11}$C-LBT-999 has been already evaluated in baboons, showing high target-to-background ratio (striatum, ~30; midbrain, ~6; and thalamus, ~2) and binding potential (striatum, ~23; midbrain, 2; and thalamus, 0.7) (*11*). However, in vitro experiments in liver microsomes and liquid chromatography–tandem mass spectrometry analysis have proposed that a labeled $^{11}$C-*N*-dealkyl metabolite is produced—a metabolite that has been suggested to have affinity for the DAT (*12*). The labeling of LBT-999 with $^{18}$F in the fluoromethylvinyl moiety would prevent the production of a labeled *N*-dealkyl metabolite binding to the DAT. The radiolabeling of $^{18}$F-LBT-999 has been already reported (*9,10*). To our knowledge, data on the quantification of $^{18}$F-LBT-999 in nonhuman primates have not been reported. In this study, we examined $^{18}$F-LBT-999 in nonhuman primates to evaluate the quantification of the binding to the DAT and to calculate estimates of whole-body radiation dose, important aspects to assess the potential of the tracer for future applications in human subjects.

## MATERIALS AND METHODS

### Nonhuman Primates

Four female rhesus monkeys (*Macaca mulatta*) for the DAT quantification and 2 female cynomolgus monkeys (*Macaca fascicularis*) for the whole-body biodistribution and radiation dosimetry were examined (Supplemental Table 1; supplemental materials are available online only at http://jnm.snmjournals.org). Rhesus monkeys were used for the DAT quantification because the study included arterial cannulation and measurement of the input function. The monkeys are owned by the Centre for Psychiatry Research, Department of Clinical Neuroscience, Karolinska Institutet, and housed in the Astrid Fagraeus Laboratory of the Swedish Institute for Infectious Disease Control, Solna, Sweden. The study was approved by the Animal Ethics Committee of the Swedish Animal Welfare Agency and was performed according to the guidelines reported by Clark et al. (*13*). In the DAT quantification study, the anesthesia was induced by intramuscular injection of ketamine hydrochloride (12 mg/kg, Ketalar; Pfizer) and maintained by the administration of a mixture of Sevoflurane (2%–8%), $O_2$, and medical air after endotracheal intubation. In the whole-body biodistribution study the anesthesia was maintained by intravenous infusion of ketamine hydrochloride (4 mg/kg/h, Ketalar) and xylazine hydrochloride (0.4 mg/kg/h, Rompun Vet.; Bayer).

### Preparation of $^{18}$F-LBT-999

LBT-999 and its chloro-LBT-999 precursor (((2*S*,3*S*)-methyl 3-(*p*-tolyl)-8-((*E*)-4-chloro-2-en-1-yl)-8-azabicyclo[3.2.1]octane-2-carboxylate)) were obtained from INSERM U930, CHRU. No-carrier-added $^{18}$F-LBT-999 was synthesized in a manner similar to previously described procedures (*10,14*). In short, $^{18}$F-LBT-999 was produced via direct nucleophilic substitution of chloro analog Cl-LBT-999 by adding 1.5–2 mg of chloro precursor dissolved in 500 μL of dimethyl sulfoxide to the dry K$^{18}$F/K(2.2.2) complex and heating the mixture at 165°C for 10 min. The mixture was subsequently cooled to room temperature, diluted with water, and purified by injection onto a C-18 μ-Bondapak (300 × 7.8 mm, 10 μm) semipreparative high-performance liquid chromatography (HPLC) column (Waters) with MeCN/0.1% aqueous trifluoroacetic acid (25:75) as mobile phase. Formulation of $^{18}$F-LBT-999 was conducted as follows. The $^{18}$F-LBT-999 fraction from HPLC was diluted in 60 mL of sterile water containing 1.0 mg of sodium ascorbate per milliliter. The resulting solution was passed though an Oasis HLB 3-mL cartridge (Waters) preconditioned by a wash with 10 mL of ethanol, followed by 10 mL of distilled water. The cartridge was washed with 10 mL of distilled water and radiotracer eluted with 1.0 mL of ethanol into a vial containing 8 mL of phosphate-buffered saline (*9*). The aliquot for the quality control analysis was then taken, and the product was filtered using a sterile Millex-GV 0.22-μm filter (Millipore). After filtration, the pH of the product was measured to confirm it was between pH 6.5 and 8. Typically, radiosynthesis took 90–110 min (including HPLC purification and formulation) with 1.5–4.5 GBq of $^{18}$F-LBT-999 prepared, with a specific activity ranging from 224 to 482 GBq/μmol (Supplemental Table 1).

### Brain PET Measurements

The head was immobilized with a fixation device (*15*). Body temperature was maintained by a Bair Hugger device (model 505; Arizant Health Care Inc.) and monitored by an oral thermometer. Electrocardiogram, heart rate, respiratory rate, oxygen saturation, and arterial blood pressure were continuously monitored throughout the experiments. In each monkey, 1 PET measurement was conducted using the HRRT system (Siemens Molecular Imaging) after intravenous administration of $^{18}$F-LBT-999 (Supplemental Table 1). A catheter was inserted in an artery of the lower limb, and arterial blood was collected continuously for 5 min using an automated blood sampling system (ABSS) at a speed of 3 mL/min (Allog AB). Blood samples (1.5 mL) were drawn at 1–10, 15, 30, 45, 60, 90, 120, 150, 180, 210, and 240 min for blood and plasma radioactivity and metabolite correction.

A 6-min transmission scan using a single $^{137}$Cs source was obtained immediately before the radioligand injection. List-mode data were acquired for 243 min. PET images were reconstructed with a series of frames of increasing duration (4 × 10, 4 × 20, 4 × 60, 7 × 180, 16 × 360, and 10 × 720 s) using the ordinary Poisson 3-dimensional ordered-subset expectation maximization algorithm, with 10 iterations and 16 subsets, including modeling of the point spread function, after correction for attenuation, random and scatter. The resolution of the reconstructed images was 1.5 mm in full width at half maximum (*16*).

### Image Analysis

Volumes of interest were delineated on coregistered PET/MR images, and delineation was guided by an atlas of 1 Rhesus monkey brain (*17*). The MR image was manually coregistered to an average PET image using the FUSION tool in the software PMOD 3.0 (PMOD Technologies). Volumes of interest for the caudate, putamen, midbrain, thalamus, cerebellum, whole brain, and skull (frontal, temporal, and occipital skull) were drawn using PMOD 3.0.

Decay-corrected time–activity curves for all regions plotted over time and radioactivity concentration were expressed as percentage standardized uptake value (SUV) and calculated as radioactivity concentration (kBq/cm$^3$)/(radioactivity injected [MBq]/body weight [kg]) × 100. The cerebellum was considered the reference region; the volumes of interest were drawn on cerebellar hemispheres, excluding the midline structure that could contain DAT binding sites (*18*).

### Radiometabolite Analysis

A reversed-phase HPLC method was used to determine the percentages of radioactivity in monkey plasma that correspond to unchanged radioligand and radiometabolites during the course of a PET measurement. The plasma (0.5 mL) obtained after centrifugation of blood at 2,000*g* for 2 min was mixed with acetonitrile (0.7 mL). The mixture was centrifuged at 2,000*g* for 2 min, and the supernatant acetonitrile–plasma mixture (1.1 mL) was injected to a radio-HPLC system. The blood (2.0 mL) and plasma (0.5 mL) were counted in a NaI well-counter. The radio-HPLC system used in the plasma experiments consisted of an interface module (D-7000; Hitachi), an L-7100 pump (Hitachi), an injector (model 7125, with a 5.0-mL loop; Rheodyne) equipped with a μ-Bondapak C18 column (300 × 7.8 mm, 10 μm; Waters), and an ultraviolet absorption detector (L-7400, 254 nm; Hitachi) in series with a dual bismuth germanium oxide coincidence radiation detector (S-2493Z; Oyokoken) equipped with a 550-μL flow cell. Acetonitrile (A) and ammonium formate (100 mM) (B) were used as the mobile phase at 6.0 mL/min, according to the following program: 0−2.0 min (A/B), 20:80 v/v; 2.0−10.0 min, 20:80→80:20 v/v; 10.0−12.0 min (A/B), 80:20 v/v; 12.0−13.0 min (A/B), 80:20→20:80 v/v; and 13.0−15.0 min (A/B), 20:80 v/v. Peaks for radioactive compounds eluting from the column were integrated and their areas expressed as a percentage of the sum of the areas of all detected radioactive compounds (decay-corrected to the time of injection on the HPLC).

### Measurement of Protein Binding

An ultrafiltration method was used to estimate the free fraction, $f_p$, of $^{18}$F-LBT-999 in plasma. Monkey plasma (500 μL) or saline solution (500 μL) as a control were mixed with $^{18}$F-LBT-999 solution (50 μL, ~1 MBq) and incubated at room temperature for 10 min. After the incubation, 200-μL portions of the incubation mixtures were pipetted into ultrafiltration tubes (Centrifree YM-30, molecular weight cutoff, 30,000; Millipore) and centrifuged at 1,500*g* for 15 min. Equal aliquots (20 μL) of the ultrafiltrate ($C_{free}$) and of the plasma ($C_{total}$) were counted for their $^{18}$F radioactivity with a NaI well-counter. Each determination was performed in duplicate. The free fraction of $^{18}$F-LBT-999 was calculated as $f_p = C_{free}/C_{total}$, and the results were corrected for the membrane binding measured with the control samples.

### Quantification

Kinetic analysis was performed with a 1-tissue-compartment model (1-TCM) and 2-tissue compartment model (2-TCM) (Supplemental Appendix 1). The goodness of fit was assessed using the $\chi^2$ (sum of the squared discrepancies between data and model predictions divided by the number of degrees of freedom) and the model selection criterion (*19*). The identifiability of parameters was expressed by the coefficient of variation (COV), which was calculated as (SE)/(estimate of the parameter) and expressed as a percentage (%COV) (*19*). The F test was used to assess whether the 2-TCM provided a significantly better fit than the 1-TCM (*20*).

The total (free + protein bound) plasma concentration of the parent was used as an input function, and the radioactivity concentration in blood was used for blood volume correction. The blood volume fraction (vB) and the time delay between the arrival of the tracer at the ABSS detector and in the brain were estimated by a preliminary fitting of the whole-brain time–activity curve with a 2-TCM. Graphical analysis (GA) was performed with the Logan plot (*21*). A time of equilibrium (t*) of 145 min was used for measuring the slope of the linear part of the Logan plot.

The outcome measures were total distribution volume ($V_T$) (DAT-rich regions) and nondisplaceable distribution volume ($V_{ND}$) (cerebellum) (*22*). The binding potentials, *BP* (binding potential relative to the free concentration of radioligand in plasma [$BP_F$] and binding potential relative to the concentration of nondisplaceable radioligand in tissue [$BP_{ND}$]), were measured using the cerebellum as a reference region (Supplemental Appendix 2). Kinetic and GAs were performed using PMOD 3.0.

### Whole-Body Distribution and Radiation Dosimetry

Whole-body PET scans were acquired using a Biograph TruePoint TrueV PET/CT system (Siemens Medical Solutions) after intravenous administration of $^{18}$F-LBT-999 (Supplemental Table 1). The body of the monkey was immobilized using a vacuum pad. Five PET/CT sessions, each covering 3 axial fields of view (AFOVs), were conducted. Before each session, a whole-body low-dose CT scan was obtained for attenuation correction. The first PET session consisted of two 30 s × 3 AFOV scans, the second PET session of three 60 s × 3 AFOV scans, the third of three 120 s × 3 AFOV scans, the fourth of three 240 s × 3 AFOV scans, and the fifth of nine 360 s × 3 AFOV scans. The time for the bed to return to the original position was approximately 60 s, and the total duration of the whole-body scan was approximately 250 min. PET images were reconstructed with an ordered-subset expectation maximization algorithm, with 4 iterations, 8 subsets, and using a 5-mm gaussian filter. Regions of interest (ROIs) were drawn on axial slices for most of the organs except for the bone, which was drawn on coronal slices, with the help of the CT part for anatomic landmarks. ROIs were drawn on the brain, parotid glands, thyroid gland, lungs, heart, left ventricle, liver, gallbladder, whole gastrointestinal tract (stomach, small intestine, and large intestine could not be separately delineated on PET/CT images), spleen, kidneys, bladder, bone (sum of sternum, claviculae, humerus, scapulae, and costae), and vertebral spine. A large ROI was drawn on the whole body for the estimation of the remainder activity. Radioactivity concentration in each PET scan was decay-corrected to the time of injection. Radioactivity was expressed as percentage of the injected radioactivity (%IA) calculated as follows: kBq/cm$^3$ × ROI volume (cm$^3$) ÷ 1,000/MBq injected × 100, and plotted versus time. Estimates of the absorbed radiation dose in humans were calculated with the OLINDA/EXM software, using the adult male (~70 kg) reference model. To estimate the dose adsorbed by the intestine, a model with a fraction of 10% entering the small intestine was used, based on the %IA measured in the whole gastrointestinal tract and using the standard gastrointestinal tract model in OLINDA/EXM. As for the bladder, a dynamic model with a fraction of 30%, a biologic half-life of 1.6–4.1 h, and a void interval of 4.8 h was used.

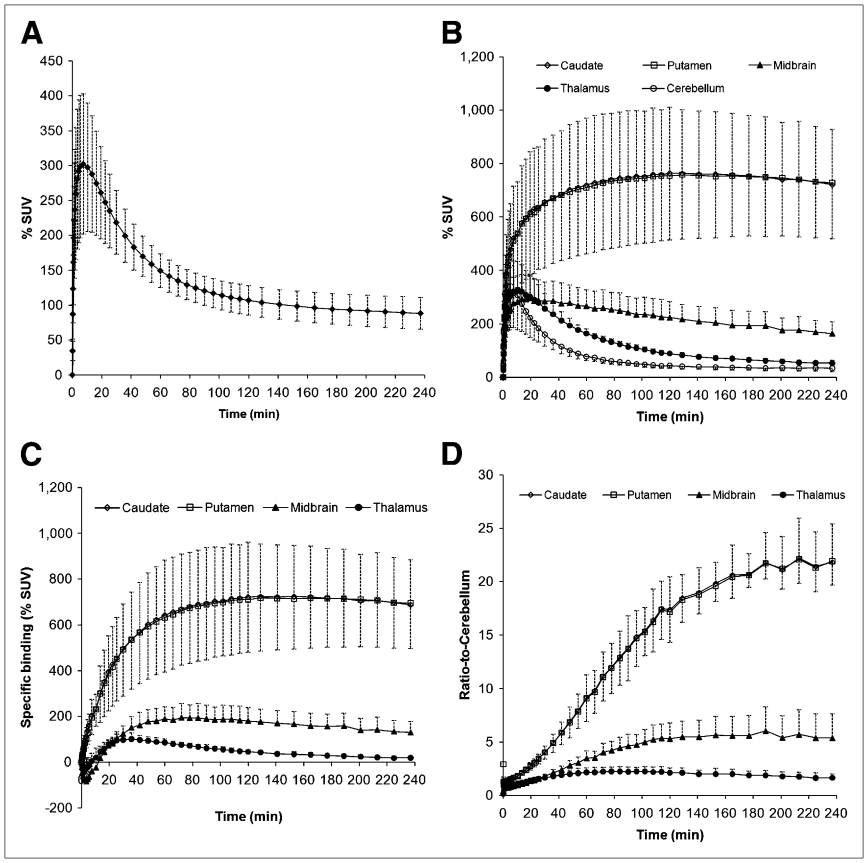


**FIGURE 1.** Mean time–activity curves (bars represent 1 SD) of $^{18}$F-LBT-999 corresponding to whole brain (A), regional uptake (B), specific binding (C), and ratio to cerebellum (D).

## RESULTS

### Brain Kinetics

Time–activity curves of $^{18}$F-LBT-999 in the brain are [**Fig. 1**] displayed in Figure 1. The average peak brain uptake of $^{18}$F-LBT-999 was approximately 300% SUV. Higher uptake was found in caudate and putamen, followed by the midbrain and thalamus. The cerebellum showed the lowest uptake. Peak specific binding (region–cerebellum) was reached at approximately 120–140 min in the striatum, 60–80 min in the midbrain, and 20–40 min in the thalamus. The ratio to the cerebellum was 20–25 in the striatum, approximately 5 in the midbrain, and 1–2 in the thalamus. A representative [**Fig. 2**] image of $^{18}$F-LBT-999 is shown in Figure 2. Moderate skull uptake was noted and measured in frontal, temporal, and occipital bone, increasing up to 300%–400% SUV (Supplemental Figs. 1 and 2). The ROIs of the cerebellum were not near the area of skull uptake, and the cerebellar radioactivity concentration was expected to receive negligible contribution from the skull uptake (Supplemental Figs. 1 and 2).

### Radiometabolite Analysis and Protein Binding

Representative high-performance liquid chromatograms obtained at 15 min after the injection of $^{18}$F-LBT-999 are [**Fig. 3**] displayed in Figure 3A. The unchanged radioligand eluted at approximately 10.5 min. There were 3 radiometabolite peaks, with retention times of 2.5 min (Met 1), 4.5 min (Met 2), and approximately 7 min (Met 3); thus, the radiometabolites were more polar than the unchanged tracer. Met 1 and Met 3 were consistently present in all monkeys. $^{18}$F-LBT-999 was rapidly metabolized (Fig. 3B), accounting for approximately 20% of the plasma radioactivity at 15 min and less than 10% at 60 min. The more polar Met 1 was the most prevalent radiometabolite peak, accounting for approximately 90% of the plasma radioactivity at 90 min after injection. On average, less than 2% of the plasma radioactivity was due to Met 3. The plasma $f_P$ was 0.33 ± 0.03.

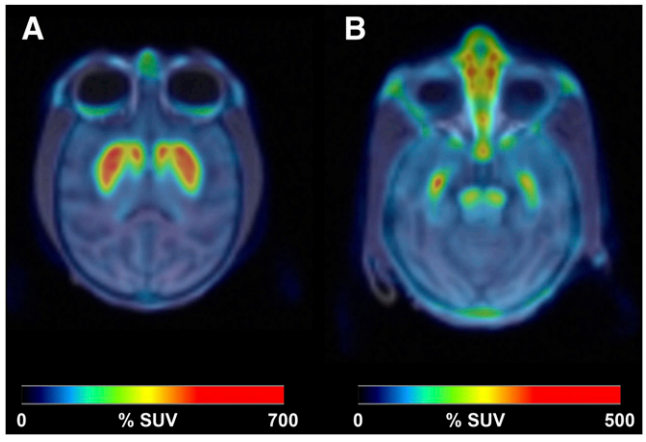


**FIGURE 2.** Representative mean image of $^{18}$F-LBT-999 from 9 to 240 min at level of striatum (A) and midbrain (B).

RGB

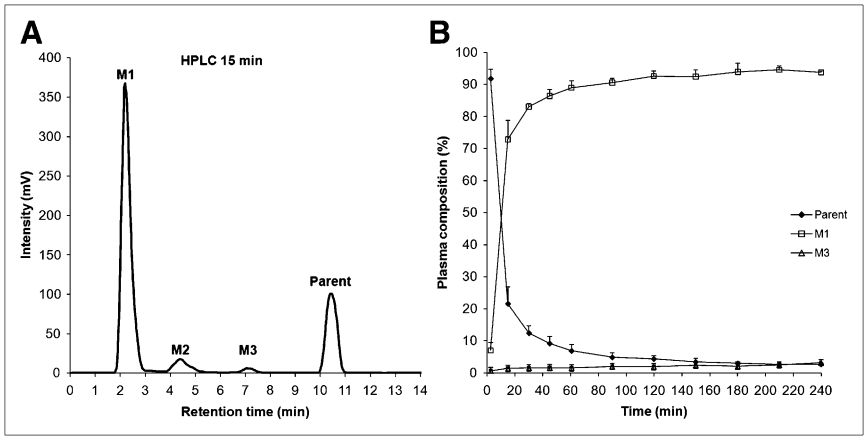


**FIGURE 3.** Representative high-performance liquid chromatogram (A) and mean plasma composition (bars represent 1 SD) after injection of $^{18}$F-LBT-999 (B).

### DAT Quantification

The average arterial input function and blood curve are shown in Figure 4. The rate constants estimated with 1-TCM and 2-TCM are displayed in Supplemental Table 2. The estimate of the delay was 10.6 ± 2.9 s (%COV, 4.8% ± 2.9%). The estimate of vB was 0.051 ± 0.003 (%COV, 10.3% ± 2.9%).

[Fig. 4]

Results of distribution volume (*DV*), $BP_F$, and $BP_{ND}$ obtained with the different methods are displayed in Tables 1–3. The 2-TCM provided higher values of $V_T$ than did the 1-TCM and was significantly better than the 1-TCM (F test, $P < 0.001$) at describing the kinetics of $^{18}$F-LBT-999 in all regions and monkeys (Fig. 5; Table 1). In monkey 3, because of slower kinetics and washout from the putamen, the estimation of $k_4$ (in the 1-TCM, 2 rate constants $K_1$ [mL·cm$^{-3}$·min$^{-1}$] and $k_2$ [min$^{-1}$] describe the exchange of the tracer between plasma and brain; in the 2-TCM, in caudate, putamen, midbrain, and thalamus, 4 rate constants $K_1$ [mL·cm$^{-3}$·min$^{-1}$], $k_2$ [min$^{-1}$], $k_3$ [min$^{-1}$], and $k_4$ [min$^{-1}$] are estimated, and $k_3$ and $k_4$ are the rate constants describing the exchange of the tracer between the nondisplaceable and the specifically bound compartments) with the 2-TCM was unreliable ($k_4$ = 0.0004 min$^{-1}$; %COV, 35.1%) and led to a high $V_T$ estimate. Therefore, $V_T$, $BP_F$, and $BP_{ND}$ in the putamen showed the highest mean and SD.

[Table 1] [Table 2] [Table 3] [Fig. 5]

The Logan GA provided estimates of $V_T$ (Table 1) lower than did the 2-TCM, by 38% ± 12% in the caudate and by 41% ± 27% in the putamen but by only 2% ± 8% in the midbrain. On the other hand, $V_T$ in the thalamus and $V_{ND}$ were, respectively, 8% ± 6% and 26% ± 17% higher than those estimated with 2-TCM. The underestimation of $BP_F$ using the Logan GA was larger in the caudate (40% ± 12%) and putamen (42% ± 27%) and lower in the midbrain (9% ± 9%) and thalamus (14% ± 29%) (Table 2). No major differences of *DV*s or *BP* were found with a t* greater than 145 min (data not shown).

Logan GA (Table 3), as compared with 2-TCM, underestimated $BP_{ND}$ in all regions (by 51% ± 13% in the caudate, by 52% ± 24% in the putamen, by 26% ± 16% in the midbrain, and by 30% ± 29% in the thalamus). Reference tissue models largely underestimated $BP_{ND}$ in the caudate and putamen (66%–69%), whereas $BP_{ND}$ was similar to 2-TCM in the midbrain and thalamus (Table 3). The simplified reference tissue model (SRTM) provided results similar to the 4-parameter (full) reference tissue model (FRTM). Logan Ref and MRTM2, as compared with the FRTM and SRTM, tended to underestimate $BP_{ND}$. No major differences of $BP_{ND}$ estimated with the Logan noninvasive approach (Logan Ref) and multilinear reference tissue model 2 (MRTM2) were found with a t* greater than 145 min (data not shown).

The influence of the duration of image analysis on the *DV* was examined by fitting the average time–activity curve for each brain region with the average input function, by removing each time point, and by refitting the data using the same starting values ($K_1$ = 0.1 mL·cm$^3$·min$^{-1}$; $k_2$ = 0.1 min$^{-1}$; $k_3$ = 0.01 min$^{-1}$; and $k_4$ = min$^{-1}$). The estimate of $V_T$ in the striatum was increasing as the duration of

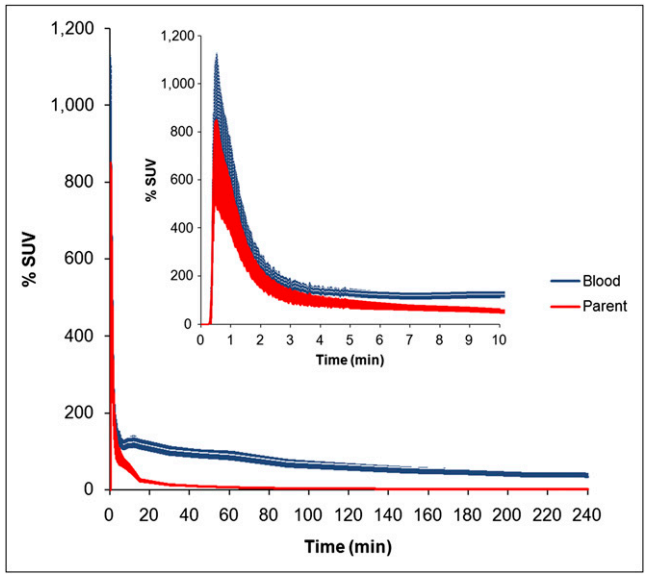


**FIGURE 4.** Mean arterial blood and plasma parent radioactivity (% SUV) (bars represent 1 SD) after injection of $^{18}$F-LBT-999.

RGB



jnm089953-pm ■ 7/11/11

**TABLE 1**
Distribution Volume Estimates of $^{18}$F-LBT-999 Using 1-TCM, 2-TCM, and Logan GA

| Model | $V_T$ | | | | $V_{ND}$ |
|---|---|---|---|---|---|
| | Caudate | Putamen | Midbrain | Thalamus | Cerebellum |
| 1-TCM | 309.3 ± 80.2 | 352.5 ± 118.1 | 31.3 ± 12.5 | 10.1 ± 2.0 | 5.0 ± 1.3 |
| 2-TCM | 508.8 ± 198.8 | 804.3 ± 726.1 | 38.2 ± 14.7 | 13.0 ± 1.4 | 8.3 ± 2.2 |
| Logan | 295.4 ± 63.8 | 333.3 ± 62.0 | 36.5 ± 12.3 | 14.0 ± 1.4 | 10.2 ± 1.7 |
| $\chi^2$ | | | | | |
| 1-TCM | 1.4 ± 0.6 | 1.2 ± 0.3 | 6.8 ± 5.6 | 9.0 ± 1.4 | 12.4 ± 4.0 |
| 2-TCM | 0.1 ± 0.0 | 0.1 ± 0.0 | 0.7 ± 0.4 | 1.1 ± 0.4 | 1.6 ± 1.0 |
| Model selection criterion | | | | | |
| 1-TCM | 3.7 ± 0.5 | 3.8 ± 0.3 | 2.1 ± 0.4 | 2.7 ± 0.2 | 3.0 ± 0.4 |
| 2-TCM | 6.1 ± 0.2 | 6.4 ± 0.4 | 4.2 ± 0.6 | 4.8 ± 0.5 | 5.1 ± 0.7 |

the image analysis decreased, mainly because of the less reliable estimation of $k_4$. On the other hand, *DV* in lower density regions and cerebellum decreased as the duration of [**Fig. 6**] image analysis decreased (Fig. 6).

### Whole-Body Distribution and Radiation Dosimetry

[**Fig. 7**] In the whole-body distribution study (Fig. 7; Supplemental Fig. 3), the highest uptake (%IA) was found in the kidneys (14% at ~1 min), brain (9.7% at ~2.5 min), intestine (9.4% at ~18 min), lungs (7% at ~1 min), and liver (6.8% at ~2.6 min). Lower uptake was found in the heart (4% at ~1 min). The bone uptake was high (9.4% at ~1 min) and remained high throughout the whole imaging time (8% at ~230 min), and the spine showed increased uptake over time (from 11% at ~1 min to 19% at ~230 min). $^{18}$F-LBT-999 was mainly eliminated through the intestine and bladder. All other organs showed a maximum uptake less than 2%. Time–activity integrals for relevant organs are shown in Supplemental Table 3. The largest adsorbed dose was found in the urinary bladder wall (0.12 mGy/MBq), followed by the thyroid (0.08 mGy/[**Table 4**] MBq) and the osteogenic cells (0.06 mGy/MBq) (Table 4). The average calculated effective dose (ED) was 0.021 mSv/MBq (Table 4).

## DISCUSSION

This study examined the in vivo quantification of $^{18}$F-LBT-999 binding to the DAT in the brain and its whole-body distribution and dosimetry in nonhuman primates. The first part of the study examined the brain quantification in the rhesus monkey. The results suggest that $^{18}$F-LBT-999 is a suitable radioligand for in vivo imaging of the DAT; however, its kinetic properties are such that in vivo quantification of the DAT in the striatum would require a long imaging time (~4 h), whereas a shorter imaging time (~2 h) could be sufficient for the quantification of the DAT in the midbrain and thalamus (Supplemental Table 4). The second part of the study examined the radiation dose estimates obtained from data in cynomolgus monkeys. The ED of $^{18}$F-LBT-999 was comparable to the one observed for other $^{18}$F-labeled radioligands and suggests that $^{18}$F-LBT-999 could be suitable for DAT imaging in human subjects.

### Brain Imaging and Quantification

In nonhuman primates, $^{18}$F-LBT-999 showed good brain uptake and a high target-to-background ratio, allowing for excellent visualization of the DAT in the striatum and extrastriatal regions. However, in the striatum $^{18}$F-LBT-999 showed slow kinetics with late peak specific binding (~120–140 min), whereas in the midbrain and thalamus, peak specific binding was reached much earlier. The kinetic analysis showed that the 2-TCM model was the preferred quantification method. Because of the low $k_4$ values and possible variability of the in vivo kinetic behavior of $^{18}$F-LBT-999, $V_T$, $BP_F$, and $BP_{ND}$ in the putamen showed high variability. Therefore, accurate quantification of the DAT in the striatum would require at least 4 h of imaging, assuming that the kinetic properties of $^{18}$F-LBT-999 would be similar in both human subjects and nonhuman primates. On the other hand, in the midbrain and the thalamus, shorter imag-

**TABLE 2**
$BP_F$ of $^{18}$F-LBT-999 Calculated Using 1-TCM, 2-TCM, and Logan GA

| Model | $BP_F$ | | | |
|---|---|---|---|---|
| | Caudate | Putamen | Midbrain | Thalamus |
| 1-TCM | 915.6 ± 245.9 | 1,028.6 ± 274.3 | 78.8 ± 35.8 | 15.3 ± 4.5 |
| 2-TCM | 1,484.5 ± 526.4 | 2,288.8 ± 1,914.9 | 89.0 ± 46.4 | 14.1 ± 7.6 |
| Logan | 852.2 ± 161.7 | 962.5 ± 112.1 | 78.6 ± 39.5 | 11.2 ± 6.4 |

**TABLE 3**
$BP_{ND}$ of $^{18}$F-LBT-999 Calculated Using 1-TCM, 2-TCM, and Logan GA and Estimated Using 4 Reference Tissue Models (FRTM, SRTM, Logan Ref, and MRTM2)

| Model | $BP_{ND}$ | | | |
|---|---|---|---|---|
| | Caudate | Putamen | Midbrain | Thalamus |
| 1-TCM | 63.1 ± 18.7 | 75.2 ± 41.2 | 5.6 ± 2.9 | 1.1 ± 0.6 |
| 2-TCM | 68.2 ± 42.7 | 120.2 ± 144.4 | 4.1 ± 2.8 | 0.7 ± 0.5 |
| Logan | 29.3 ± 10.8 | 32.9 ± 11.0 | 2.8 ± 1.6 | 0.4 ± 0.3 |
| FRTM | 19.4 ± 2.9 | 19.8 ± 1.9 | 3.2 ± 1.4 | 0.7 ± 0.3 |
| SRTM | 19.6 ± 3.1 | 19.8 ± 1.9 | 3.2 ± 1.4 | 0.7 ± 0.3 |
| Logan Ref | 18.1 ± 3.1 | 18.8 ± 2.4 | 3.1 ± 1.4 | 0.7 ± 0.3 |
| MRTM2 | 18.1 ± 2.9 | 18.8 ± 2.3 | 3.2 ± 1.5 | 0.7 ± 0.3 |

ing times could be sufficient for accurate quantification. When the different models were compared with the 2-TCM, the underestimation of $V_T$ or $BP_{ND}$ was larger in the caudate and putamen than in the midbrain and thalamus. Taken together, these findings suggest that $^{18}$F-LBT-999 could be particularly suitable for imaging and quantification of the DAT in extrastriatal regions. All reference tissue methods provided similar estimates of $BP_{ND}$, slightly higher for the FRTM and SRTM than for Logan Ref and MRTM2. The underestimation of *DV*s and $BP_{ND}$ using graphical analyses or reference tissue models has already been reported for $^{11}$C-PE2I (*23*). We attempted to use a t* greater than 145 min in GA, but the estimation of the outcome measures did not improve, possibly because a lower number of time points and higher noise were included. As for the reference tissue models, and particularly the SRTM, a possible reason for the discrepancy could be the violation of the assumption of a 1-TCM for the target and the reference regions.

The only available quantification data have been reported for $^{11}$C-LBT-999 using 1-TCM and invasive Logan GA and SRTM using cerebellum as reference region (*11*). In the case of $^{11}$C-LBT-999, it has been reported that $k_3$ and $k_4$ were poorly identified with 2-TCM (*11*). With $^{18}$F-LBT-999, we had the possibility to image until 4 h and we have shown that, with the exception of 1 monkey, $k_3$ and $k_4$ could be adequately identified and that the 1-TCM did not seem to be a suitable quantification model. *DV*s of $^{18}$F-LBT-999 with Logan GA were approximately 1.4–2 times higher than *DV*s of $^{11}$C-LBT-999, probably because of more rapid elimination and a lower plasma concentration of $^{18}$F-LBT-999. $BP_{ND}$ of $^{18}$F-LBT-999 with SRTM was approximately 10%–20% lower than the $BP_{ND}$ of $^{11}$C-LBT-999 in the striatum, whereas it was approximately 30% higher in the midbrain and similar in the thalamus. The differences in $BP_{ND}$ could be related to the nonhuman primate species (rhesus vs. baboon), to the methodology used (a HRRT vs. HR+, different ROI templates), and to the differences in metabolism of the radioligands.

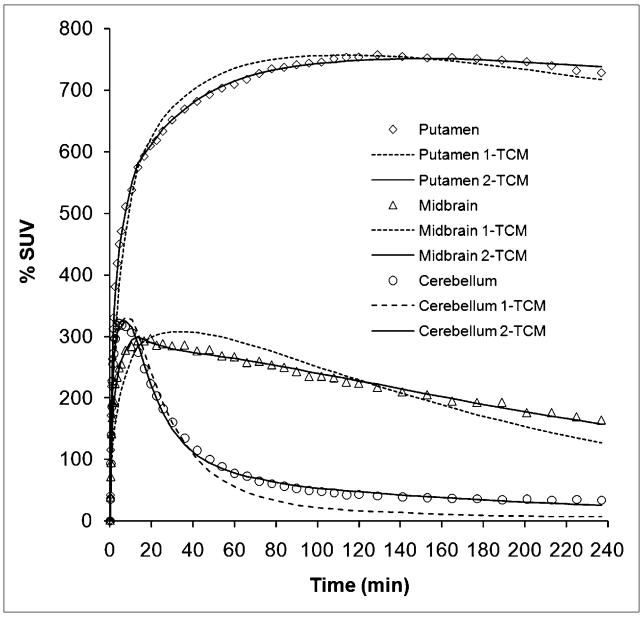


**FIGURE 5.** Comparison of fitting with 1-TCM or 2-TCM.

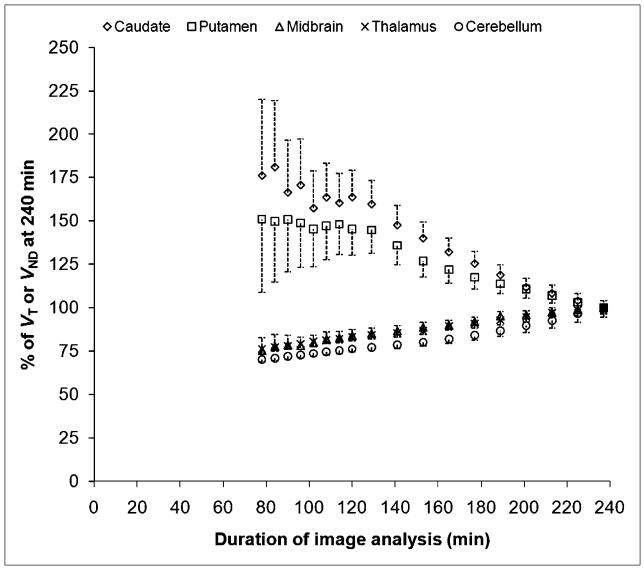


**FIGURE 6.** Relationship between distribution volume and duration of image analysis.

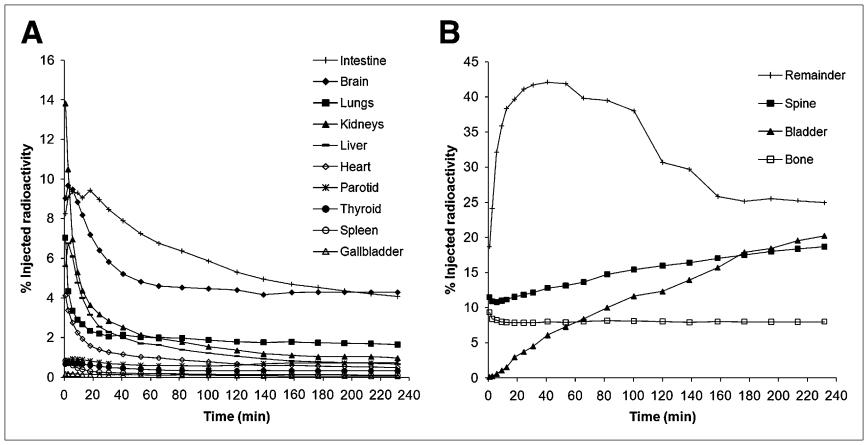


**FIGURE 7.** Uptake of $^{18}$F-LBT-999 (percentage injected dose) in different organs (A), reminder of body, spine, bone, and bladder (B).

### Radiometabolite Analysis

In this study, consistently 1 polar (Met 1, ~90% at 90 min) and 1 less polar radiometabolite peak (Met 2, ~2% at 90 min) were observed. Ex vivo data of the radiometabolites of $^{18}$F-LBT-999 are not available, but if Met 1 is a $^{18}$F-fluoro-alkyl analog, as previously suggested (*12*), it might enter the brain and contribute to the nondisplaceable binding. To investigate more in this direction, we examined the time stability of the *DV* in the different brain regions. The pattern of time-dependent *DV* change of $^{18}$F-LBT-999 was similar to another DAT radioligand, $^{18}$F-FECNT, in which $^{18}$F-fluoroethanol has been found to enter the brain and contribute to the nondisplaceable binding (*24*). However, if the outcome measure of interest is $BP_{ND}$ the degree of underestimation in low-density regions and cerebellum seems to be similar (Fig. 6), perhaps producing less bias in $BP_{ND}$. Another possible explanation of the time-dependent change of *DV* would be that the parent radioligand is metabolized and trapped in the brain. However, we believe that trapping in the brain is unlikely to occur because the binding of $^{11}$C-LBT-999, which is structurally equivalent to $^{18}$F-LBT-999, has been shown to be reversibly displaced by PE2I (*11*).

**TABLE 4**
Radiation Dose Estimates of $^{18}$F-LBT-999 for Different Organs

| Target organ | Total dose (mGy/MBq) | | Mean total dose (mGy/MBq) |
|---|---|---|---|
| | Monkey 5 | Monkey 6 | |
| Urinary bladder wall | 0.088 | 0.144 | 0.116 |
| Thyroid | 0.088 | 0.078 | 0.083 |
| Osteogenic cells | 0.075 | 0.048 | 0.061 |
| Upper large intestine wall | 0.038 | 0.046 | 0.042 |
| Small intestine | 0.034 | 0.041 | 0.038 |
| Kidneys | 0.043 | 0.030 | 0.036 |
| Brain | 0.028 | 0.023 | 0.026 |
| Red marrow | 0.027 | 0.018 | 0.023 |
| Lower large intestine wall | 0.017 | 0.020 | 0.018 |
| Heart wall | 0.020 | 0.013 | 0.017 |
| Uterus | 0.012 | 0.015 | 0.014 |
| Lungs | 0.013 | 0.010 | 0.012 |
| Gallbladder wall | 0.011 | 0.011 | 0.011 |
| Ovaries | 0.010 | 0.012 | 0.011 |
| Spleen | 0.010 | 0.008 | 0.009 |
| Liver | 0.010 | 0.007 | 0.008 |
| Total body | 0.009 | 0.008 | 0.008 |
| Adrenals | 0.007 | 0.005 | 0.006 |
| Pancreas | 0.006 | 0.005 | 0.005 |
| Muscle | 0.005 | 0.005 | 0.005 |
| Stomach wall | 0.005 | 0.004 | 0.005 |
| Testes | 0.004 | 0.005 | 0.004 |
| Thymus | 0.004 | 0.003 | 0.003 |
| Skin | 0.003 | 0.003 | 0.003 |
| Breasts | 0.003 | 0.002 | 0.002 |
| ED equivalent (mSv/MBq) | 0.027 | 0.028 | 0.027 |
| ED (mSv/MBq) | 0.021 | 0.022 | 0.021 |

### Whole-Body Dosimetry Study

The whole-body distribution study showed that the main routes of excretion of $^{18}$F-LBT-999 are the urinary and gastrointestinal systems, with the bladder being the critical organ. High uptake was found in the bone, and accumulation of $^{18}$F-LBT-999 was found in the vertebral bone and the skull, with a relatively large dose estimated for the osteogenic cells. The degree of uptake in the bone and in the skull could be different in human subjects. From the imaging perspective, the uptake in the skull does not seem to be a limitation, because the primary brain regions (striatum, midbrain, thalamus, and the reference cerebellum) are not near the bone. From the dosimetry aspect, the dose to the osteogenic cells (0.061 mGy/MBq) and to the red marrow was somewhat higher than the dose previously reported for other $^{18}$F-labeled radioligands such as $^{18}$F-FP-CIT (0.005–0.007 mGy/MBq in bone surfaces and red marrow) (*25*) or $^{18}$F-SPAR-Q (0.02–0.03 mGy/MBq) (*26*). Although the estimates of the dose for the osteogenic cells and the red marrow were relatively high, the estimates of ED were in the same range as other $^{18}$F-labeled radioligands including $^{18}$F-FDG (0.024–0.027 mSv/MBq) (*27*). Therefore, considering that the limit of ED in several European Union countries is within 5 and 10 mSv (*28*), the amount of administered

radioactivity of $^{18}$F-LBT-999 would be close to 480 MBq, allowing also for more than 1 injection per year.

## CONCLUSION

In nonhuman primates $^{18}$F-LBT-999 seems to be a suitable PET radioligand for the quantification of the DAT, particularly in extrastriatal regions, such as the midbrain and the thalamus. In the striatum, because of the slow washout, at least 4 h of imaging seem to be required for the quantification. However, those findings need to be confirmed in human subjects. The estimates of radiation dose are within the values previously reported for other $^{18}$F-labeled PET radioligands. The uptake in the bone and the skull, albeit providing relatively high doses to osteogenic cells and red marrow, does not seem to be a limitation in terms of imaging and radiation exposure and could be different in human subjects.

## DISCLOSURE STATEMENT

The costs of publication of this article were defrayed in part by the payment of page charges. Therefore, and solely to indicate this fact, this article is hereby marked "advertisement" in accordance with 18 USC section 1734.

## ACKNOWLEDGMENTS

We thank Gudrun Nylen and the staff of the PET Centre and Nuclear Medicine for excellent assistance in the conduction of the PET and PET/CT studies. The study has been supported by Cyclopharma Laboratoires, by the FP6-project DiMI LSHB-CT-2005-512146 and by the Région Centre program "Radex." No other potential conflict of interest relevant to this article was reported.

## REFERENCES

1. Girault JA, Greengard P. The neurobiology of dopamine signaling. *Arch Neurol.* 2004;61:641–644.
2. Ciliax BJ, Drash GW, Staley JK, et al. Immunocytochemical localization of the dopamine transporter in human brain. *J Comp Neurol.* 1999;409:38–56.
3. Varrone A, Halldin C. Molecular imaging of the dopamine transporter. *J Nucl Med.* 2010;51:1331–1334.
4. Jucaite A, Fernell E, Halldin C, Forssberg H, Farde L. Reduced midbrain dopamine transporter binding in male adolescents with attention-deficit/hyperactivity disorder: association between striatal dopamine markers and motor hyperactivity. *Biol Psychiatry.* 2005;57:229–238.
5. Arakawa R, Ichimiya T, Ito H, et al. Increase in thalamic binding of [$^{11}$C]PE2I in patients with schizophrenia: a positron emission tomography study of dopamine transporter. *J Psychiatr Res.* 2009;43:1219–1223.
6. Chalon S, Hall H, Saba W, et al. Pharmacological characterization of (*E*)-*N*-(4-fluorobut-2-enyl)-2beta-carbomethoxy-3beta-(4′-tolyl)nortropane (LBT-999) as a highly promising fluorinated ligand for the dopamine transporter. *J Pharmacol Exp Ther.* 2006;317:147–152.
7. Emond P, Guilloteau D, Chalon S. PE2I: a radiopharmaceutical for in vivo exploration of the dopamine transporter. *CNS Neurosci Ther.* 2008;14:47–64.
8. Dollé F, Emond P, Mavel S, et al. Synthesis, radiosynthesis and in vivo preliminary evaluation of [$^{11}$C]LBT-999, a selective radioligand for the visualisation of the dopamine transporter with PET. *Bioorg Med Chem.* 2006;14:1115–1125.
9. Dollé F, Hinnen F, Emond P, et al. Radiosynthesis of [$^{18}$F]LBT-999, a selective radioligand for the visualization of the dopamine transporter with PET. *J Labelled Comp Radiopharm.* 2006;49:687–698.
10. Dollé F, Helfenbein J, Hinnen F, et al. One-step radiosynthesis of [$^{18}$F]LBT-999: a selective radioligand for the visualization of the dopamine transporter with PET. *J Labelled Comp Radiopharm.* 2007;50:716–723.
11. Saba W, Valette H, Schollhorn-Peyronneau MA, et al. [$^{11}$C]LBT-999: a suitable radioligand for investigation of extra-striatal dopamine transporter with PET. *Synapse.* 2007;61:17–23.
12. Schollhorn-Peyronneau MA, Saba W, Valette H, et al. Metabolism of LBT-999, [$^{11}$C]-LBT-999 and [$^{18}$F]-LBT-999, a selective ligand for PET examination of the dopamine transporter. Paper presented at: European Association of Nuclear Medicine (EANM); September 30–October 4, 2006; Athens.
13. Clark JD, Gebhart GF, Gonder JC, Keeling ME, Kohn DF. Special report: the 1996 guide for the care and use of laboratory animals. *ILAR J.* 1997;38:41–48.
14. Ryzhikov NN, Seneca N, Krasikova RN, et al. Preparation of highly specific radioactivity [$^{18}$F]flumazenil and its evaluation in cynomolgus monkey by positron emission tomography. *Nucl Med Biol.* 2005;32:109–116.
15. Karlsson P, Farde L, Halldin C, et al. PET examination of [$^{11}$C]NNC 687 and [$^{11}$C]NNC 756 as new radioligands for the D1-dopamine receptor. *Psychopharmacology (Berl).* 1993;113:149–156.
16. Varrone A, Sjoholm N, Eriksson L, Gulyas B, Halldin C, Farde L. Advancement in PET quantification using 3D-OP-OSEM point spread function reconstruction with the HRRT. *Eur J Nucl Med Mol Imaging.* 2009;36:1639–1650.
17. Saleem KS, Logothesis NK. *A Combined MRI and Histology Atlas of the Rhesus Monkey Brain in Stereotaxic Coordinates*. 1st ed. Oxford, U.K.: Academic Press; 2007.
18. Melchitzky DS, Lewis DA. Tyrosine hydroxylase- and dopamine transporter-immunoreactive axons in the primate cerebellum: evidence for a lobular- and laminar-specific dopamine innervation. *Neuropsychopharmacology.* 2000;22:466–472.
19. Fujita M, Seibyl JP, Verhoeff NP, et al. Kinetic and equilibrium analyses of [$^{123}$I] epidepride binding to striatal and extrastriatal dopamine $D_2$ receptors. *Synapse.* 1999;34:290–304.
20. Carson RE. Parameter estimation in PET. In: Phelps M, Schelbert H, eds. *Positron Emission Tomography and Autoradiography: Principles and Applications for the Brain and the Heart.* New York, NY: Raven Press; 1986:287–346.
21. Logan J, Fowler JS, Volkow ND, et al. Graphical analysis of reversible radioligand binding from time-activity measurements applied to [N-$^{11}$C-methyl]-(-)-cocaine PET studies in human subjects. *J Cereb Blood Flow Metab.* 1990; 10:740–747.
22. Innis RB, Cunningham VJ, Delforge J, et al. Consensus nomenclature for in vivo imaging of reversibly binding radioligands. *J Cereb Blood Flow Metab.* 2007; 27:1533–1539.
23. Jucaite A, Odano I, Olsson H, Pauli S, Halldin C, Farde L. Quantitative analyses of regional [$^{11}$C]PE2I binding to the dopamine transporter in the human brain: a PET study. *Eur J Nucl Med Mol Imaging.* 2006;33:657–668.
24. Zoghbi SS, Shetty HU, Ichise M, et al. PET imaging of the dopamine transporter with $^{18}$F-FECNT: a polar radiometabolite confounds brain radioligand measurements. *J Nucl Med.* 2006;47:520–527.
25. Robeson W, Dhawan V, Belakhlef A, et al. Dosimetry of the dopamine transporter radioligand $^{18}$F-FPCIT in human subjects. *J Nucl Med.* 2003;44:961–966.
26. Sprague DR, Chin FT, Liow JS, et al. Human biodistribution and radiation dosimetry of the tachykinin NK1 antagonist radioligand [$^{18}$F]SPA-RQ: comparison of thin-slice, bisected, and 2-dimensional planar image analysis. *J Nucl Med.* 2007;48:100–107.
27. Deloar HM, Fujiwara T, Shidahara M, et al. Estimation of absorbed dose for 2-[F-18]fluoro-2-deoxy-D-glucose using whole-body positron emission tomography and magnetic resonance imaging. *Eur J Nucl Med.* 1998;25:565–574.
28. Verbruggen A, Coenen HH, Deverre JR, et al. Guideline to regulations for radiopharmaceuticals in early phase clinical trials in the EU. *Eur J Nucl Med Mol Imaging.* 2008;35:2144–2151.